On the Processing of Single-Pass InSAR Data for Accurate Elevation Measurements of Ice Sheets and Glaciers

Andreas Benedikter, *Member, IEEE*, Marc Rodriguez-Cassola, Pau Prats-Iraola, *Senior Member, IEEE*, Gerhard Krieger, *Fellow, IEEE*, and Georg Fischer

***Abstract*— Single-pass interferometric synthetic aperture radar (InSAR) elevation measurements of dry snow, firn, and ice are known to be substantially biased downward due to a partial penetration of the radar signals into the medium, resulting in a phase center location within the volume. The so-called penetration bias, i.e., the elevation difference between surface and InSAR phase center, can be estimated from the contribution of the volume to the interferometric coherence and may be used to retrieve the surface elevation. In this article, we show that both an additional elevation bias and a horizontal shift occur in the InSAR processing for natural media with a dielectric constant different to the one of air, originating from an uncompensated stretch of the vertical wavenumber in the medium and refraction effects at the surface. This geolocation error depends on the magnitude of the penetration bias, the dielectric constant, and the acquisition geometry. It may reach up to few meters for X- and C-band frequencies and more for lower frequencies and therefore may significantly affect cryospheric elevation products from past (SRTM), current (TanDEM-X), and future (e.g., Harmony and Tandem-L) SAR interferometers. In this article, the geolocation error is assessed and an adapted interferometric processing allowing for an accurate geolocation (i.e., surface elevation measurement) is presented.**

***Index Terms*— Cryosphere, elevation bias, geocoding, glaciers, Harmony, ice sheets, penetration bias, synthetic aperture radar (SAR), SAR interferometry, TanDEM-X.**

I. Introduction

DIGITAL elevation models (DEMs) generated with single-pass interferometric synthetic aperture radar (InSAR) are a fundamental source for mapping the surface elevation and topographic changes over ice sheets and glaciers [1]. The nonnegligible penetration of radar signals into snow, firn, and ice at commonly used frequency bands, e.g., from P to X band, results in an elevation bias of the backscatter phase center versus the actual surface, typically described in the literature as penetration bias. In other words, the DEM generated from InSAR data does not replicate the surface, but it is biased downward [1], [2], [3], [4], [5], [6], [7], [8], [9], [10], [11].

Manuscript received 8 May 2023; revised 18 October 2023 and 21 November 2023; accepted 16 December 2023. Date of publication 21 December 2023; date of current version 19 January 2024. This work was supported in part by the European Space Agency under Contract 4000135083/21/NL/FF/ab. *(Corresponding author: Andreas Benedikter.)*

The authors are with the Microwaves and Radar Institute, German Aerospace Center (DLR), 82234 Weßling, Germany (e-mail: andreas.benedikter@dlr.de).

Digital Object Identifier 10.1109/TGRS.2023.3345415

In this article, we report that there is a systematic difference between the physical phase center height and the apparent phase center height measured with InSAR. This difference results from propagation effects within the glacial volume that are not accounted for in conventional InSAR processing, in particular, from a vertical wavenumber stretch in the glacial volume and refraction effects at the surface, both a direct consequence of the larger dielectric permittivity of snow, firn, and ice compared to the permittivity of air, resulting in a reduced propagation velocity. The relation between the surface height h_s, the physical height of the phase center h_{pc}, and the apparent phase center height measured with conventionally processed InSAR $h_{\mathrm{InSAR,c.}}$ can be approximated as

$$h_s \approx h_{pc} + \Delta h \approx h_{\mathrm{InSAR,c.}} - \Delta h_2 + \Delta h \tag{1}$$

where Δh is the physical penetration bias (assumed positive, according to the convention in [2] and [3]) and Δh_2 (assumed negative for biases oriented downward) represents an additional bias resulting from the abovementioned wavenumber stretch, from here on referred to as propagation bias. A comparable propagation bias effect has been reported in [12], resulting from propagation effects through the atmosphere. Commonly, Δh_2 is neglected and the assumption is that the surface height, h_s, is related to $h_{\mathrm{InSAR,c.}}$ via

$$\widetilde{h_s} \approx h_{\mathrm{InSAR,c.}} + \Delta h \tag{2}$$

where $\widetilde{\cdot}$ is used because we show in this article that the formulation does not result in an accurate surface height estimate. The approximation in (2) has been used in several research works, where the physical penetration bias Δh is estimated as the difference between an InSAR DEM (i.e., $h_{\mathrm{InSAR,c.}}$) and a surface reference DEM (i.e., h_s) generated with, e.g., optical sensors that do not penetrate the surface, to evaluate the penetration of the signals and to retrieve information on snow, firn, and ice properties [1], [4], [5], [6], [7], [8], [9]. Vice versa [5], [10], and [11] have used the inversion strategies of [2] and [3] to estimate the penetration bias Δh from the interferometric coherence to retrieve the surface elevation h_s from the TanDEM-X DEM (i.e., $h_{\mathrm{InSAR,c.}}$). Since Δh_2 is a direct consequence of the propagation through the glacial volume, it should not be neglected, but properly addressed whenever penetration into the volume occurs, especially when considering future single-pass SAR interferometers operating in lower frequency bands. Examples are Tandem-L (L band)

[13] and the Earth Explorer 10 mission Harmony (C band) [14] that is partly focused on generating elevation and elevation change products over land ice on a global scale.

It is important to note that both the penetration into the volume and the uncompensated change in propagation velocity do not only result in an elevation bias, but also a shift in horizontal, i.e., ground range, direction, as also noted in [12] in the case of propagation effects through the atmosphere. For retrieving accurate elevation estimates in cases of a spatially fast-changing topography, this horizontal shift needs to be taken into account. Hence, the DEM generation for the propagation through several media should be formulated in terms of a 3-D geolocation problem that is best addressed within the interferometric processing rather than in a secondary elevation correction.

In Section II, the geolocation error is assessed and quantified, whereas in Section III, adapted InSAR processing strategies are presented that provide an accurate geolocation for the cases in which the InSAR DEM should replicate the surface elevation or the phase center elevation. Section IV presents results generated with the Harmony End-To-End Performance Simulator (HEEPS) [15], and conclusions are drawn in Section V.

II. Assessment of the Geolocation Error

Part of a standard interferometric processing chain is shown in Fig. 1, illustrating the process from the interferogram to the retrieved DEM. The geolocation problem for glaciers and ice sheets arises within the geocoding of the interferometric information. The geocoding is commonly performed by a numerical computation of the 3-D intersect point of the interferometric phase, the range sphere, and the Doppler cone by solving the following set of equations for each pixel of the absolute phase, $\phi_{\text{abs.}}$, [16]:

$$\begin{cases} \phi_{\text{abs.}} = \dfrac{4\pi}{\lambda} \cdot \left(\left| \mathbf{p} - \mathbf{s}_{\text{p}} \right| - \left| \mathbf{p} - \mathbf{s}_{\text{s}} \right| \right) \\ r_{\text{p}} = \left| \mathbf{p} - \mathbf{s}_{\text{p}} \right| \\ f_{\text{DC,p}} = \dfrac{2}{\lambda \cdot r_{\text{p}}} \cdot \mathbf{v}_{\text{p}} \cdot \left(\mathbf{p} - \mathbf{s}_{\text{p}} \right) \end{cases} \tag{3}$$

where r_{p} is the slant range of the primary acquisition, $f_{\text{DC,p}}$ is the Doppler centroid of the primary acquisition, λ is the wavelength, $\mathbf{p}$ is the unknown point on ground, $\mathbf{s}_{\text{p}}$ is the position of the primary satellite, $\mathbf{s}_{\text{s}}$ is the position of the secondary satellite, and $\mathbf{v}_{\text{p}}$ is the velocity vector of the primary satellite.

Since for standard application scenarios, there is no a priori information on the penetration bias (i.e., the phase center depth), nor the surface elevation, free-space propagation of the radar signals between the sensor and the scatterer is typically assumed. This necessarily leads to a misinterpretation of the interferometric phase and the range for cases in which the phase center is located within the volume, because the signals experience an additional delay that is caused by the reduced propagation velocity due to the permittivity of the glacial volume.

Fig. 2 shows a simple simulation of the geocoding process and the resulting error. A simplified two-layer model (free space and glacial volume) with a constant permittivity within each layer is assumed and used in the derivations throughout this article. As an example, a horizontal snow surface, a satellite altitude of 700 km, a constant relative permittivity of the glacial volume of $\varepsilon_{\text{r}} = 2.0$, and a phase center depth of 10 m are assumed. Note that the phase center can be interpreted as the center of gravity of the backscatter distribution along the elevation direction within the volume. The blue lines represent contours of constant fast time (solid line) and interferometric phase (dashed line) when correctly accounting for the reduced propagation velocity within the volume. The contours are computed using a numerical ray tracing, based on Fermat's principle of least time. The red lines represent the equivalent contours assuming propagation only through air, i.e., the assumption made in the standard interferometric geocoding, corresponding to the first two equations in (3). Note that an acquisition geometry with a Doppler centroid equal to zero is assumed here. The shift between the blue intersect point (p_{s}) and the red one (p_{a}) represents the geolocation error, i.e., the error in the retrieved DEM. Note that the error is independent of the interferometric baseline (further discussed below) but has a strong dependence on the incident angle at the surface. Both a shift in height and ground range are present, with magnitudes depending on the phase center depth, the incident angle, and the permittivity.

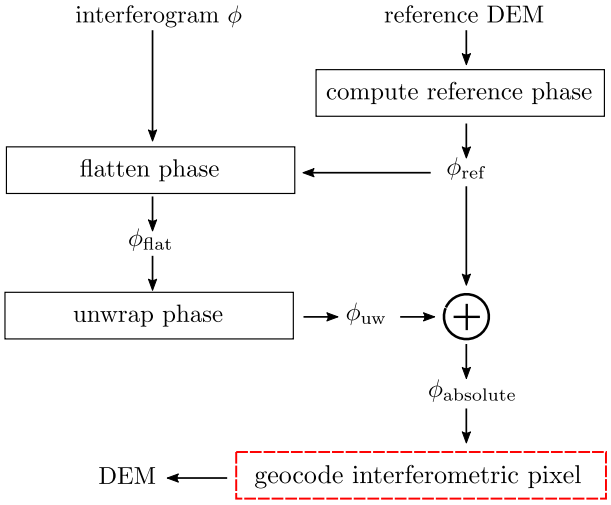

Fig. 1. Standard interferometric processing chain for generating a DEM. Calibration steps are omitted for simplicity.

For the simple propagation model used in the simulation of Fig. 2, the height error, i.e., the propagation bias Δh_2, may be quantified by evaluating the change in the interferometric vertical wavenumber k_z when propagating into the firn volume. The vertical wavenumber is stretched when penetrating in the dielectric denser medium. It can be written in terms of k_z as [17], [18]

$$k_{z,\text{vol}} = k_z \cdot \sqrt{\varepsilon_{\text{r}}} \cdot \frac{\cos\theta_{\text{i}}}{\cos\theta_{\text{r}}} \tag{4}$$

where θ_{i} is the local incident angle and θ_{r} is the refraction angle that can be computed using Snell's law. The physical contribution of the penetrated firn volume Δh (i.e., the height difference between the surface and the phase center) to the

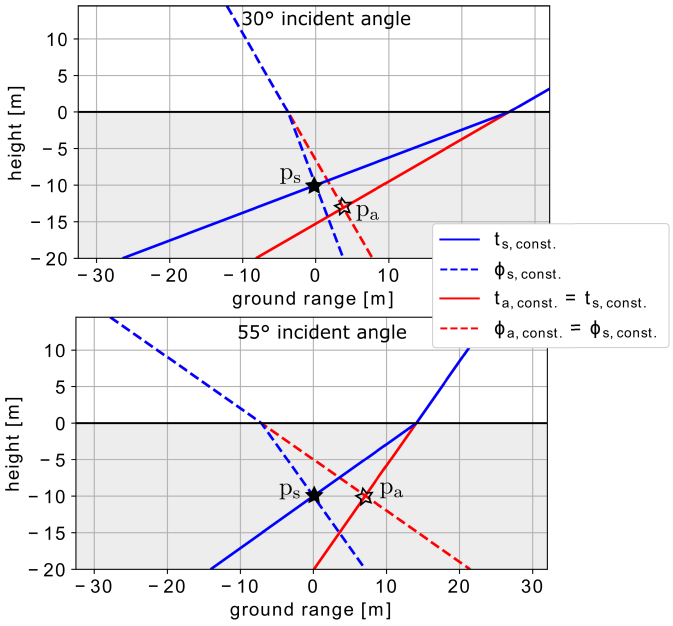

Fig. 2. Illustrative simulation of the geocoding process and the resulting geolocation error for a flat surface. Blue lines show contours of constant fast time (solid) and interferometric phase (dashed) when accounting for the propagation effects into the volume. Red lines show the corresponding contours for a free-space assumption. The shift between the blue intersect point (p_s) and the red one (p_a) represents the geolocation error.

interferometric phase can be written as $\phi_{\text{pen}} = \Delta h \cdot k_{z,\text{vol}}$. When assuming propagation through free space in the InSAR processing, ϕ_{pen} is erroneously scaled with k_z and not $k_{z,\text{vol}}$. Hence, the propagation bias Δh_2 resulting from the free-space assumption in processing may be formulated as

$$\Delta h_2 \approx \frac{\Delta h \cdot k_{z,\text{vol}}}{k_{z,\text{vol}}} - \frac{\Delta h \cdot k_{z,\text{vol}}}{k_z} = \Delta h \cdot \left(1 - \sqrt{\varepsilon_\text{r}} \cdot \frac{\cos\theta_\text{i}}{\cos\theta_\text{r}}\right). \tag{5}$$

Note again that all dependencies with the interferometric baseline cancel out. A geometrical derivation may be found when considering the interferometric pair as part of an antenna array that radiates power in the form of a collimated beam that is refracted into the glacial volume (see Fig. 3). Since the optical path lengths (i.e., the travel times) for both the physically correct propagation and the free-space assumption have to be the same, the geolocation error can be determined using the geometrical relations shown in Fig. 3, resulting in

$$\Delta h_2 = \Delta h \cdot \left(1 - \sqrt{\varepsilon_\text{r}} \cdot \frac{\cos\theta_\text{i}}{\cos\theta_\text{r}}\right) \tag{6}$$

$$\Delta r_\text{g} = \Delta h \cdot \tan\theta_\text{r} \cdot \left(\sqrt{\varepsilon_\text{r}} \cdot \frac{\sin\theta_\text{i}}{\sin\theta_\text{r}} - 1\right). \tag{7}$$

A similar derivation is provided in [19] for the SAR tomography case. Note that the expression for Δh_2 is equivalent to the wavenumber derivation in (5).

The vertical and horizontal geolocation errors are plotted in Fig. 4 as a function of the incident angle and for three different values of the penetration bias Δh. A permittivity of $\varepsilon_\text{r} = 2.0$ is assumed, representing dry firn. It is interesting to note that the

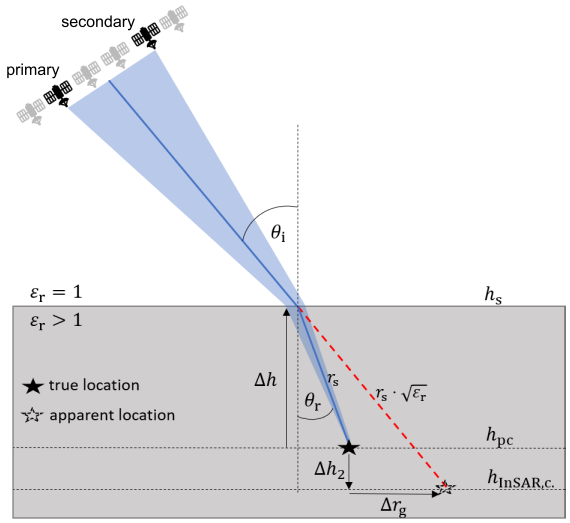

Fig. 3. Illustration for deriving the height and ground range error. The heights in the figure can be related to (1). The geometry is comparable to the 30° incident angle case in Fig. 2. For shallower incident angles, $h_\text{InSAR,c.}$ increases (see Fig. 2) and eventually surpasses the physical phase center height h_pc.

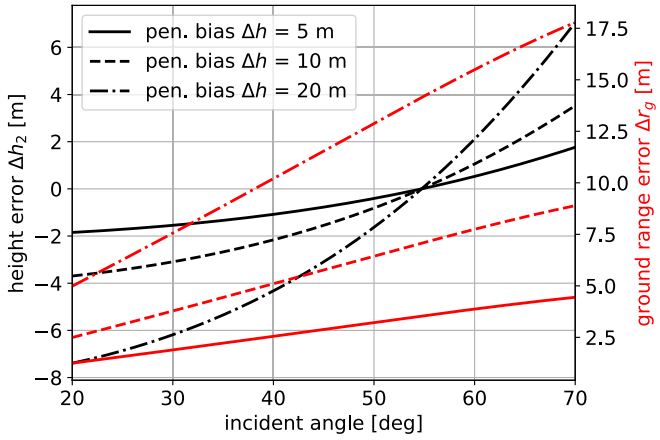

Fig. 4. Height and ground range error for different incident angles and three different penetration biases, i.e., phase center depths. A permittivity of $\varepsilon_\text{r} = 2.0$ is assumed. Note that the penetration bias corresponds to the phase center depth with respect to the surface height. A varying phase center depth may result from a varying vertical backscatter distribution in the volume or acquisition geometry.

intersect point of the Δh_2 curves is solely a function of the permittivity. Note also that even for the limited penetration reported for X band sensors (e.g., in [10]) down to 8–10 m, geolocation errors of several meters can be expected. Note that for the analysis above, a constant permittivity of the glacial volume is assumed. A more complex permittivity distribution may be accommodated by an effective mean value representing the volume above the phase center that may change depending on the phase center depth.

Using a backscatter model to characterize the glacial volume, the geolocation error can be linked to physical properties of the volume. For example, in [2], a model for describing the contribution of a uniform volume with exponential extinction properties to the complex interferometric coherence is given

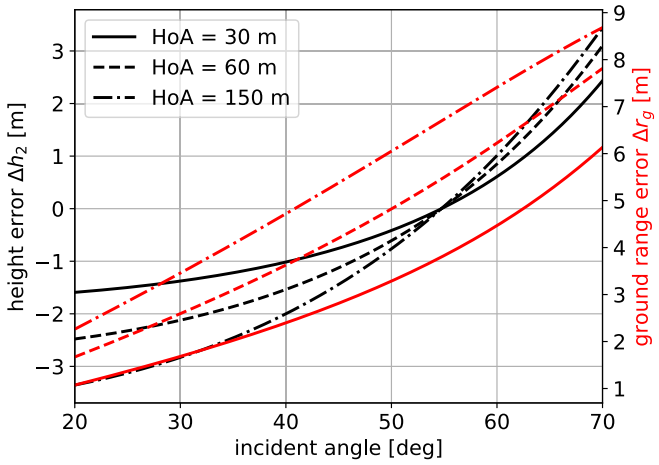

Fig. 5. Height and ground range error for different incident angles and three different heights of ambiguity. A uniform volume with a penetration depth of 10 m and a permittivity of $\varepsilon_r = 2.0$ are assumed.

as follows:

$$\gamma_{\text{vol}} = \frac{1}{1 + \text{j} \cdot 2 \cdot \pi \cdot {}^{d_2}/_{\text{HoA}_{\text{vol}}}} \tag{8}$$

where j is the imaginary unit, d_2 is the two-way penetration depth [i.e., the depth after which the power is decreased by a factor of $(1/e)$], and $\text{HoA}_{\text{vol}} = \frac{2\pi}{k_{z,\text{vol}}}$ is the height of ambiguity in the volume. From (8), the penetration bias Δh for a uniform volume can be formulated in terms of d_2 [3]

$$\Delta h = \arctan\left(k_{z,\text{vol}} \cdot d_2\right) \cdot \frac{1}{k_{z,\text{vol}}}. \tag{9}$$

Using the formulations in (6), (7), and (9), the geolocation errors are shown in Fig. 5 for a penetration depth of $d_2 = 10$ m and three heights of ambiguity (HoA) in free space. The error for the uniform volume model is dependent on the interferometric baseline (i.e., the HoA) since the transformation from d_2 to Δh results in larger Δh values for smaller baselines.

III. Adapted Processing

In this section, we present adapted processing approaches capable of accounting for both the penetration itself and the propagation related errors presented in Section II. Two application scenarios are addressed, in which the estimated topography should replicate: 1) the phase center elevation or 2) the surface elevation. It is assumed that an accurate estimate of the penetration bias, Δh, is available, for example, by means of the inversion strategies presented in [2] and [3] that are based on the measured coherence. Note that these inversions only provide a model-based estimate of Δh with limited accuracy and may introduce systematic errors in the final DEM.

A. Topographic Height Correction

A straightforward approach is to extend the conventional processing chain in Fig. 1 by a simple elevation correction step after the DEM generation to compensate the penetration bias, Δh, and the propagation bias, Δh_2, corresponding to the relation given in (1). A DEM that approximates the phase center height can be retrieved from the conventionally processed DEM, $\text{DEM}_{\text{InSAR,c.}}$, by

$$\begin{aligned}\text{DEM}_{\text{pc}} &= \text{DEM}_{\text{InSAR,c.}} - \Delta h_2 \\ &= \text{DEM}_{\text{InSAR,c.}} - \Delta h \cdot \left(1 - \sqrt{\varepsilon_r} \cdot \frac{\cos\theta_i}{\cos\theta_r}\right)\end{aligned} \tag{10}$$

whereas a DEM approximating the surface elevation is given by

$$\begin{aligned}\text{DEM}_{\text{s}} &= \text{DEM}_{\text{InSAR,c.}} + \Delta h - \Delta h_2 \\ &= \text{DEM}_{\text{InSAR,c.}} + \Delta h \cdot \sqrt{\varepsilon_r} \cdot \frac{\cos\theta_i}{\cos\theta_r}.\end{aligned} \tag{11}$$

$\text{DEM}_{\text{InSAR,c}}$, DEM_{pc}, and DEM_{s} correspond to the heights introduced in (1): $h_{\text{InSAR,c.}}$, h_{pc}, and h_{s}, respectively. Note that such simple elevation correction does not account for the shift in ground range direction, Δr_g, and may, therefore, result in residual elevation errors for areas with strong topographic gradients.

B. Adapted InSAR Processing for Surface and Phase Center Elevation Measurement

As hinted above, penetration and propagation effects need to be accounted for within the InSAR processing. The most accurate solution is to adapt the geocoding process to incorporate the refraction at the surface and the reduced propagation velocity within the volume. However, such adaption results in a significantly higher computational complexity since the ray tracing through a multilayer medium has to be done numerically.

We suggest to perform the correction by means of a compensation of the penetration phase and a correction of the range delay in terms of an adaption of the range equation within the geocoding formalism in (3). The geocoding can then be performed conventionally, assuming free space. The adapted chain is illustrated in Fig. 6. The general approach is applicable for both the generation of a surface DEM and for a phase center DEM. Only the formulations for the computation of the phase compensation and range offsets differ.

The compensation of the penetration phase contribution ϕ_{pen} needs to account for the difference between the interferometric phase at the physical position of the phase center and the surface or phase center position for a free-space assumption. For the surface case, ϕ_{pen} can be computed as

$$\phi_{\text{pen,surface}} = -\Delta h \cdot k_{z,\text{vol}}. \tag{12}$$

For the phase center case, ϕ_{pen} can be approximated as

$$\phi_{\text{pen,pc}} = \Delta h_2 \cdot k_z. \tag{13}$$

The penetration phase can then be simply used as an offset to the absolute phase, as illustrated in Fig. 6. The range shifts may be corrected in terms of an offset on the range equation of the interferometric geocoding in (3). Again, the adaption of the range equation needs to account for the difference between the range to the physical position of the phase center and the surface or phase center position assuming free space. The range offsets can be approximated as

$$\Delta r_{\text{surface}} \approx -\sqrt{\varepsilon_r} \cdot \frac{\Delta h}{\cos\theta_r} \tag{14}$$

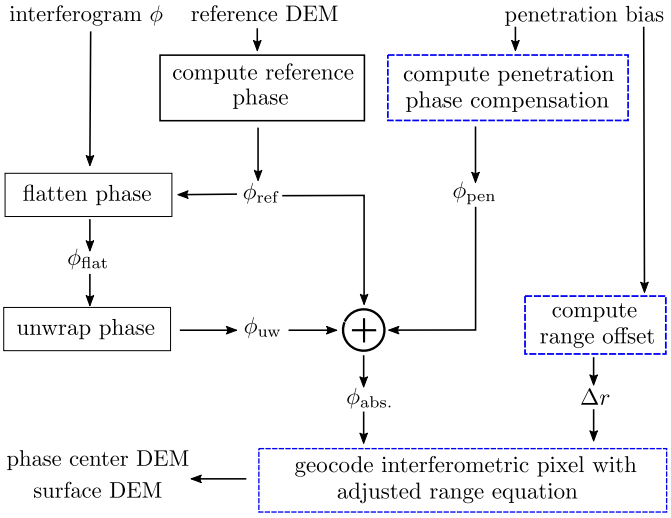

Fig. 6. Adapted interferometric processing chain for generating a DEM corresponding to the surface or the phase center, including a correction of the interferometric phase and range offsets.

TABLE I
SIMULATION PARAMETERS

Parameter	Description / Value
orbit	polar, circular, 700 km altitude
surface height	WGS 84 ellipsoid
incident angle (mean)	40°
phase center depth, Δh	-14 m to -4 m
permittivity of the penetrated volume, ε_{r}	2.0, constant

and

$$\Delta r_{\text{pc}} \approx \frac{\Delta h}{\cos\theta_{\text{r}}} \cdot (1 - \sqrt{\varepsilon_{\text{r}}}). \tag{15}$$

To apply the correction, the range equation in (3) is rewritten as

$$r_{\text{p}} + \Delta r_{\text{i}} = \left|\mathbf{p} - \mathbf{s}_{\text{p}}\right| \tag{16}$$

where the index i indicates the range offset for the surface or the phase center in (14) and (15), respectively.

Alternatively, instead of adapting the range equation in (3), the range offsets can be accounted for by interpolating the absolute phase to an adjusted range grid. Note that this approach leads to an increased computational burden and is only mentioned here since it may provide an easier integration into an existing InSAR processor.

Note that both the adaption of the range equation as well as the interpolation of the absolute phase to an adjusted range grid are first-order approximations, based on the assumption that the slope of the terrain is constant between the phase center position and the intersect point on the surface.

C. Accuracy Analysis

In order to illustrate the accuracy of the proposed approaches, they are compared within a simple simulation to an exact geocoding procedure that accounts for the refraction and propagation effects in the volume. The relevant simulation parameters are depicted in Table I. To facilitate an exact geocoding that incorporates the dielectric medium change, the surface height corresponds to the WGS 84 ellipsoid, without additional topography. The phase center height is varying between -14 and -4 m. In Fig. 7(a), the geodetic coordinates of the phase center and surface intersect points are illustrated. The coordinates correspond to the radar coordinates of a 2 km $\times$ 2 km acquisition and are computed using a Newton backgeocoding algorithm as described in [20]. Note that the backgeocoding is adapted to account for the dielectric medium change. Fig. 7(b) shows the phase center elevation in radar coordinates, and Fig. 7(c) shows the slope of the phase center elevation in range direction. The slopes up to 12 % are likely to resemble an extreme case of phase center elevation variability. However, note that the strong elevation variability may account for the effects introduced by a realistic surface topography that is absent in this simulation. Fig. 7(d) and (e) show the range offsets when comparing the correct range (resulting from the backgeocoding procedure) to the range when assuming free space, Fig. 7(d) for the phase center DEM case and Fig. 7(e) for the surface DEM case. The offsets in Fig. 7(d) are solely a consequence of the reduced propagation velocity and refraction, whereas the offsets in Fig. 7(e) additionally include the geometric distance between the surface intersect point and the phase center, together reaching up to 22 m for the present example. In the following, the resulting height errors when assuming free space in the geocoding are assessed for the cases in which the standard height correction [see (2)] is performed, or the corrections presented in Sections III-A and III-B of this work.

1) The height errors after the standard elevation correction in (2), i.e., when neglecting the propagation bias and the range offsets, are shown in Fig. 7(f) and (g) for the surface and phase center DEM case, respectively. Note that no correction is performed for the phase center DEM case. The height errors are a superposition of the erroneous height correction and the geodetic position mismatch resulting from the uncompensated range offsets (i.e., the height is not constant in the area spanned by the range offsets). The contribution due to the range offsets is stronger for the surface DEM case.
2) Fig. 7(h) and (i) show the residual height errors when applying the adapted height correction according to (10) and (11). The height estimation improved compared to the standard correction. Still, errors in the meter range are present. The residual errors can be exclusively attributed to the range offsets that translate into height errors for a topography with nonnegligible slope, as described for the previous case. Note that the pattern of the height errors resembles the one of the slopes in Fig. 7(c). For a flat topography and a constant penetration bias, no height errors would remain.
3) Fig. 7(j) and (k) show the residual height errors after applying the phase and range offset correction as described in Section III-B. The correction is not perfect because it is only a first-order approximation. Note that range offsets of few decimeters are remaining after the range correction (not explicitly shown in Fig. 7). However, even for the strong elevation variability of the present example, only height errors of few cm are still present. These are almost two orders of magnitude smaller than common height accuracy requirements.

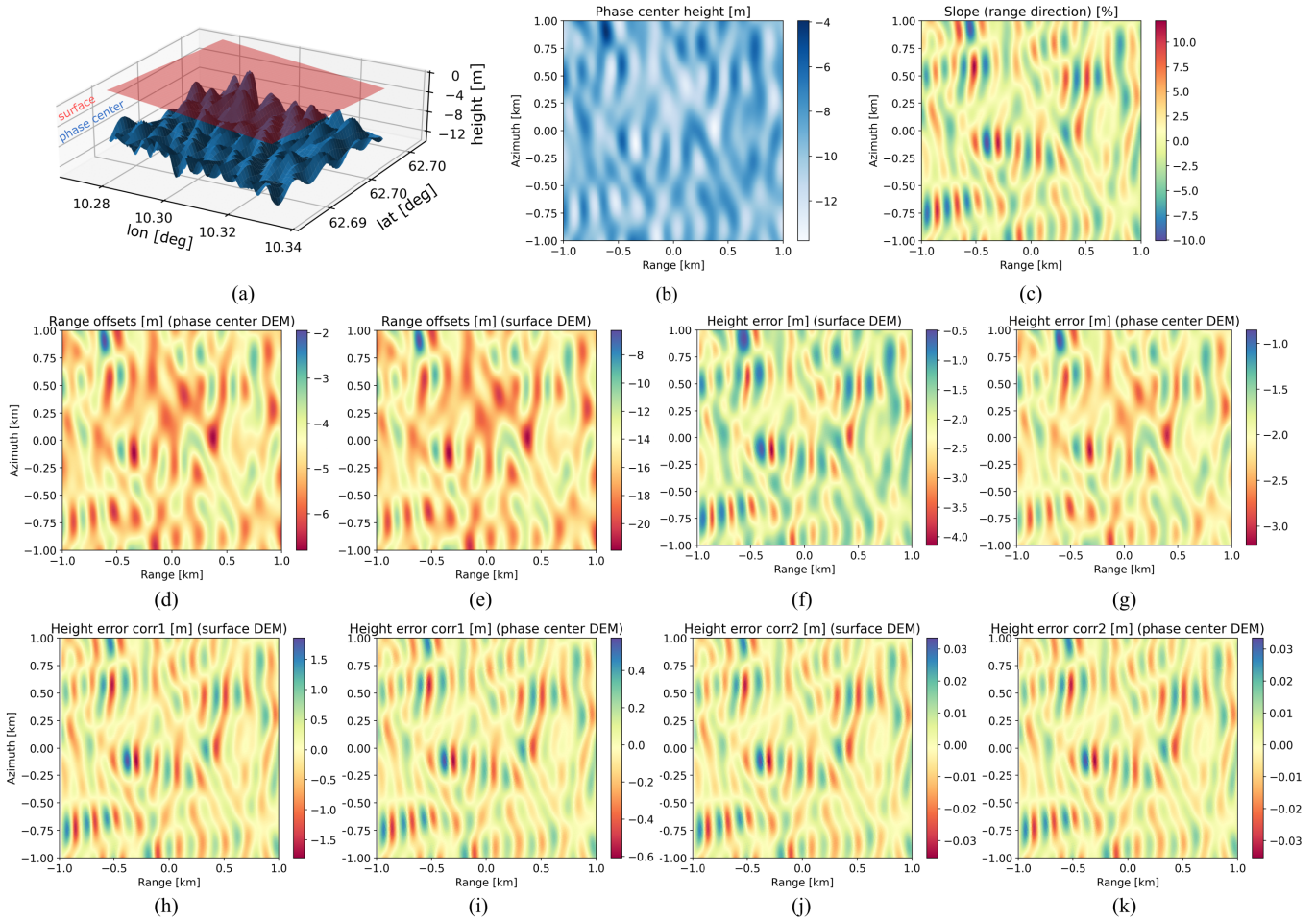

Fig. 7. Simulation for assessing the accuracy of the adapted processing approaches showing: (a) geodetic coordinates of the phase center and surface intersect points; (b) phase center elevation; (c) slope of the phase center elevation; (d) and (e) range offset between the apparent phase center position (assuming free-space propagation) and the physical phase center or the surface position, respectively; (f) and (g) height error when applying the standard elevation correction in (2) for retrieving the surface or phase center, respectively; (h) and (i) height error when applying the adapted height correction described in Section III-A; and (j) and (k) height error when applying the adapted InSAR processing described in Section III-B. Note the different range of the colorbars when comparing (h)–(k).

The discussed simulation results in Fig. 7 suggest that a height correction is not sufficient for terrains with modest to steep slopes or a spatially fast varying penetration bias. The adapted processing, as described in Section III-B, provides accurate results, even for a strongly varying topography, if a precise estimate of the penetration bias, Δh, is available.

As hinted above, biased estimates of Δh can result in systematic errors of the final DEM. Such biases may be present for heterogeneous parts of glaciers and ice sheets where model-based inversions may not replicate well enough the physical scattering and propagation properties of the glacial volume, but are expected to be small (i.e., smaller than the propagation bias, Δh_2) for rather homogeneous terrain (e.g., over the large ice sheets). Since, in the general application case with no reference date, there is no means of determining if the estimation of Δh is biased and in which direction it is biased, we suggest to always perform the adapted processing (i.e., account for the propagation bias and the range offsets) because it allows a physically correct accommodation of the propagation effects and, on average, will lead to improved elevation products.

The analyses in this article are simplified to a zero-squint acquisition geometry. For very large squint angles, also a significant geolocation error in azimuth direction is to be expected, resulting from both the incorrect geocoding and uncompensated phase residuals (due to the propagation through the glacial volume) in the SAR processing [21]. However, even for large squints of several degrees, the offsets in azimuth are marginal compared to the range offsets.

IV. Simulation Results

A reliable demonstration of the outlined effects and the proposed processing adaption on real InSAR data is challenging because a reference measurement or estimation of the penetration bias, i.e., the phase center depth, using approaches such as the inversion of the volume coherence is known to be model-dependent [22], [23]. This would necessarily result in a speculative interpretation of the results. Nevertheless, it is important to show on as much realistic as possible SAR data that the outlined effects may significantly degrade the InSAR elevation measurements of a cryospheric SAR mission.

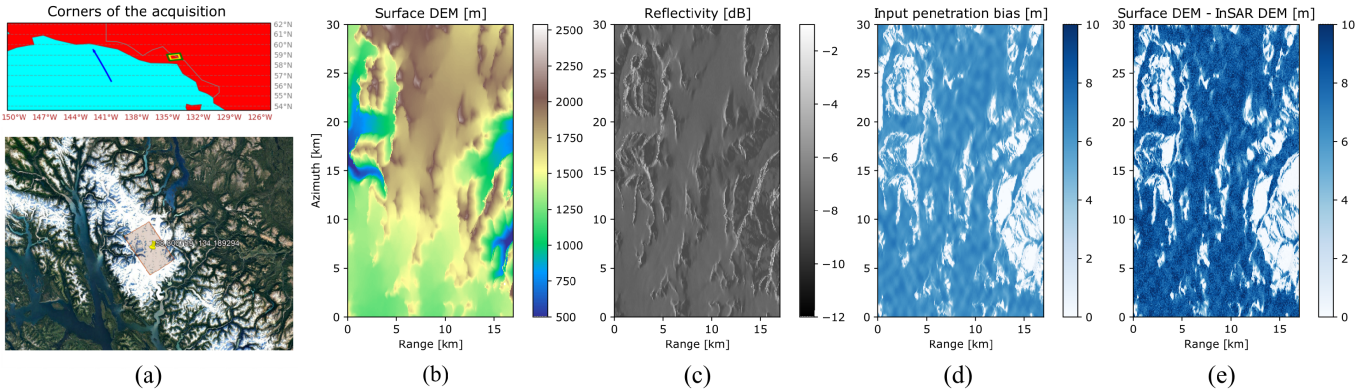

Fig. 8. Some inputs and results for the end-to-end simulation using HEEPS, showing: (a) location of the scene; (b) DEM representing the surface; (c) simulated reflectivity of the scene; (d) input penetration bias; and (e) difference between the surface DEM and the generated InSAR DEM using a conventional InSAR processing chain assuming free-space propagation.

TABLE II
HEEPS SIMULATION PARAMETERS

Parameter	Description / Value
frequency	5.405 GHz
SLC resolution (az x rg)	20 m x 5 m
interferogram resolution (az x rg)	100 m x 100 m
incident angle (mean)	30°
height of ambiguity (mean)	60 m
NESZ (mean)	−20 dB
penetration depth	0 m to 12 m
permittivity ε_r	1.8, constant
reflectivity	−12 dB to −1 dB

We use the HEEPS [15] to generate realistic SAR images and higher level products according to the Harmony system parameters. The HEEPS is based on a bistatic end-to-end (BiE2E) simulator, developed at the German Aerospace Center (DLR), Weßling, Germany [24]. The BiE2E is an integrated InSAR simulation tool with bistatic and multistatic capabilities composed of three main parts: 1) a distributed SAR raw data simulation block; 2) level 1 and level 2 processing chains; and 3) a performance evaluation module. The BiE2E allows for the efficient simulation of interferometric stacks over wide distributed areas with an exact accommodation of bistatic geometries, antenna patterns, instrument and platform effects, as well as configurable complex correlations between the simulated scenes.

The simulation parameters are chosen according to the bistatic Sentinel-1/Harmony antenna and noise behavior. The relevant simulation parameters are listed in Table II. The simulation is performed for a scene located in a mountainous glacier region in BC, Canada. The location is shown in Fig. 8(a). The glacier region is chosen as an example case. The proposed techniques are equivalently applicable to ice sheets. We use the SRTM DEM [shown in Fig. 8(b)] as the surface reference. Within the scene generation module of the raw data generator of the BiE2E, a semiphysical representation of the scene reflectivity is generated [see Fig. 8(c)] and the penetration into the glacial volume is simulated. The firn is modeled according to a uniform volume model with a varying two-way penetration depth, d_2, and a constant relative permittivity. For

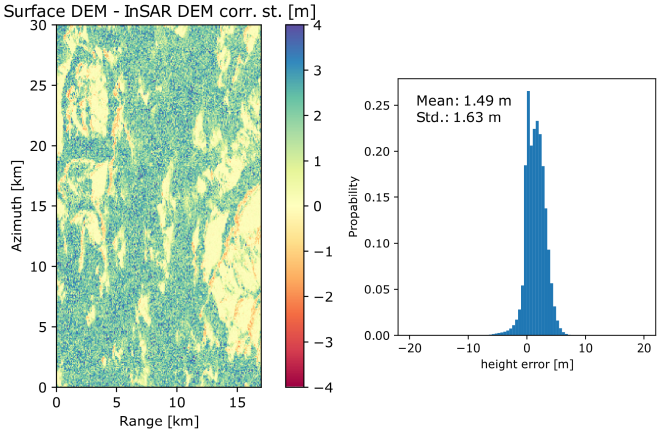

Fig. 9. Height error when applying the standard elevation correction in (2). Note the significant residual bias over the glacial areas.

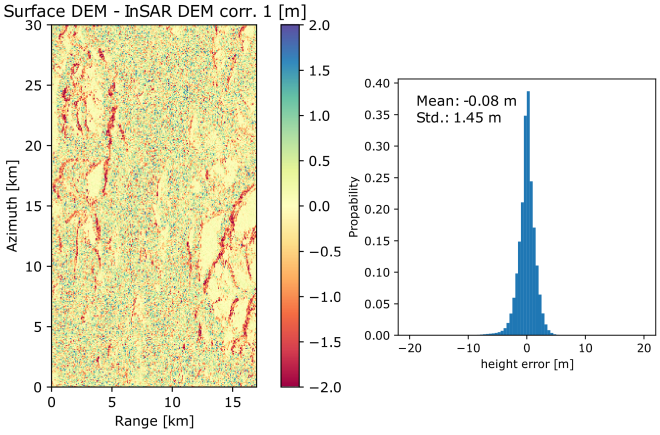

Fig. 10. Height error when applying the adapted height correction described in Section III-A. No range correction is applied.

the given local incident angles and the height of ambiguity of 60 m, the resulting penetration bias is shown in Fig. 8(d). The penetration into the glacial volume is modeled in terms of range offsets and a complex volume coherence according to the formulation in (8). The coherence is injected in the two scenes of the interferometric pair by means of a two-image

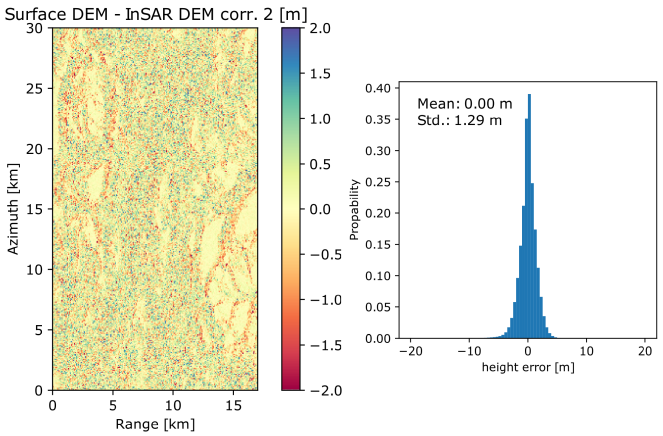

Fig. 11. Height error when applying the adapted InSAR processing described in Section III-B. Note that almost all systematic errors are removed.

Cholesky decomposition. After the scene generation and an error incorporation step (navigation, attitude, clock, etc.), the raw data are synthesized using a reverse SAR processor. Subsequently, the raw data are focused and an InSAR processor is used to generate the interferogram and DEM. For the case in which free-space propagation is assumed within the InSAR processing and no further corrections are performed, Fig. 8(e) shows the difference between the surface DEM (used as input to the simulator) and the generated InSAR DEM. Note the clear height error compared to the input penetration bias in Fig. 8(d), a direct consequence of the propagation effects into the firn volume.

Fig. 9 shows the residual height error when retrieving a surface DEM from the InSAR DEM using the standard height correction according to (2), i.e., when neglecting the propagation bias. A height offset up to 3 m over the firn areas is visible, resulting in a mean height error of 1.49 m. Note the two peaks in the histogram, corresponding to surface areas (centered around 0 m) and firn areas (centered around roughly 2.5 m). Several areas with systematic negative height offsets are visible in regions with sudden changes in the penetration bias. Those height offsets can be attributed to the uncompensated range offsets. Fig. 10 shows the results when the adapted height correction in (11) is applied, i.e., also the propagation bias is accounted for. Most of the height offsets are removed. However, the negative biases due to the range offsets are still present. Note that smaller systematic biases due to range offsets are also present in the firn areas, but not visible due to the higher phase noise caused by the volume decorrelation effects. Fig. 11 shows the results for the case in which the adapted processing, discussed in Section III-B, is applied. Almost all systematic biases have been removed. This can also be noted in the mean error of 0 m and a reduced standard deviation compared to the previous case in Fig. 10.

V. Conclusion

In this article, a bias effect (additional to the well-known penetration bias) on single-pass InSAR elevation products of glaciers and ice sheets is reported. The bias is a direct consequence of the commonly uncompensated propagation effects of the radar signals through the glacial volume, i.e., a reduced propagation velocity and refraction at the glacial surface, resulting in a 3-D geolocation error during InSAR DEM processing. If a precise estimate of the penetration bias, i.e., the phase center depth, is available, the 3-D geolocation error can be accurately corrected by means of an adapted geocoding (accounting for the propagation effects) or a compensation of the interferometric phase and range offset that are inherent to the propagation through the volume. A simple height correction may be sufficient for scenes with moderate topography. Even though the bias has not been explicitly reported in data-based research work, it should be taken into account in the generation of cryospheric elevation products from SAR interferometers (e.g., TanDEM-X, Harmony, and Tandem-L), whenever penetration into the volume occurs. Elevation errors (additional to the well-known penetration bias) up to a few meters are to be expected in C and X bands, and beyond 10 m in L band. It is important to note that the proposed processing approaches do not solve the problem of precisely estimating the penetration bias. Still, even for inaccurate penetration bias estimates, they should be applied, whenever penetration into the glacial volume occurs since they allow a physically correct accommodation of the propagation effects and, on average, will lead to improved elevation products.

Comparable propagation effects should also be observable for arid areas, where the radar signals penetrate into sand or dry soil. The problem statement can be generalized to natural media with different dielectric properties than air that are transparent or semitransparent at microwave frequencies and is applicable to delays introduced by the troposphere and ionosphere.

Acknowledgment

The authors would like to thank the two anonymous reviewers for their effort and valuable suggestions.

References

[1] E. Berthier et al., "Measuring glacier mass changes from space—A review," *Rep. Prog. Phys.*, vol. 86, no. 3, pp. 8–12, 2023.

[2] H. A. Zebker and E. W. Hoen, "Penetration depths inferred from interferometric volume decorrelation observed over the Greenland ice sheet," *IEEE Trans. Geosci. Remote Sens.*, vol. 38, no. 6, pp. 2571–2583, Nov. 2000.

[3] J. Dall, "InSAR elevation bias caused by penetration into uniform volumes," *IEEE Trans. Geosci. Remote Sens.*, vol. 45, no. 7, pp. 2319–2324, Jul. 2007.

[4] S. Abdullahi, B. Wessel, M. Huber, A. Wendleder, A. Roth, and C. Kuenzer, "Estimating penetration-related X-band InSAR elevation bias: A study over the Greenland ice sheet," *Remote Sens.*, vol. 11, no. 24, p. 2903, Dec. 2019.

[5] P. Rizzoli, M. Martone, H. Rott, and A. Moreira, "Characterization of snow facies on the Greenland ice sheet observed by TanDEM-X interferometric SAR data," *Remote Sens.*, vol. 9, no. 4, p. 315, Mar. 2017.

[6] B. Wessel et al., "TanDEM-X PolarDEM 90 m of antarctica: Generation and error characterization," *Cryosphere*, vol. 15, no. 11, pp. 5241–5260, Nov. 2021.

[7] A. Dehecq, R. Millan, E. Berthier, N. Gourmelen, E. Trouvé, and V. Vionnet, "Elevation changes inferred from TanDEM-X data over the Mont-Blanc area: Impact of the X-band interferometric bias," *IEEE J. Sel. Topics Appl. Earth Observ. Remote Sens.*, vol. 9, no. 8, pp. 3870–3882, Aug. 2016.

[8] A. Lambrecht, C. Mayer, A. Wendt, D. Floricioiu, and C. Völksen, "Elevation change of Fedchenko glacier, Pamir Mountains, from GNSS field measurements and TanDEM-X elevation models, with a focus on the upper glacier," *J. Glaciol.*, vol. 64, no. 246, pp. 637–648, Aug. 2018.

[9] Y. Dong, J. Zhao, D. Floricioiu, L. Krieger, T. Fritz, and M. Eineder, "High-resolution topography of the Antarctic peninsula combining the TanDEM-X DEM and reference elevation model of Antarctica (REMA) mosaic," *Cryosphere*, vol. 15, no. 9, pp. 4421–4443, Sep. 2021.

[10] H. Rott et al., "Penetration of interferometric radar signals in Antarctic snow," *Cryosphere*, vol. 15, no. 9, pp. 4399–4419, Sep. 2021.

[11] C. Sommer, T. Seehaus, A. Glazovsky, and M. H. Braun, "Brief communication: Increased glacier mass loss in the Russian high Arctic (2010–2017)," *Cryosphere*, vol. 16, no. 1, pp. 35–42, Jan. 2022.

[12] G. Krieger, F. De Zan, M. Bachmann, P. L. Dekker, M. R. Cassola, and J. S. Kim, "Tropospheric and ionospheric effects in spaceborne single-pass SAR interferometry and radargrammetry," in *Proc. 10th Eur. Conf. Synth. Aperture Radar*, Jun. 2014, pp. 1–4.

[13] A. Moreira et al., "Tandem-L: A highly innovative bistatic SAR mission for global observation of dynamic processes on the Earth's surface," *IEEE Geosci. Remote Sens. Mag.*, vol. 3, no. 2, pp. 8–23, Jun. 2015.

[14] P. López-Dekker, H. Rott, P. Prats-Iraola, B. Chapron, K. Scipal, and E. D. Witte, "Harmony: An earth explorer 10 mission candidate to observe land, ice, and ocean surface dynamics," in *Proc. IEEE Int. Geosci. Remote Sens. Symp.*, Jul. 2019, pp. 8381–8384.

[15] M. Rodriguez-Cassola et al., "End-to-end level-0 data simulation tool for future spaceborne SAR missions," in *Proc. 12th Eur. Conf. Synth. Aperture Radar*, Jun. 2018, pp. 1–6.

[16] E. Sansosti, "A simple and exact solution for the interferometric and stereo SAR geolocation problem," *IEEE Trans. Geosci. Remote Sens.*, vol. 42, no. 8, pp. 1625–1634, Aug. 2004.

[17] J. J. Sharma, I. Hajnsek, K. P. Papathanassiou, and A. Moreira, "Estimation of glacier ice extinction using long-wavelength airborne pol-InSAR," *IEEE Trans. Geosci. Remote Sens.*, vol. 51, no. 6, pp. 3715–3732, Jun. 2013.

[18] Y. Lei, P. Siqueira, and R. Treuhaft, "A dense medium electromagnetic scattering model for the InSAR correlation of snow," *Radio Sci.*, vol. 51, no. 5, pp. 461–480, May 2016.

[19] S. Tebaldini, T. Nagler, H. Rott, and A. Heilig, "Imaging the internal structure of an Alpine glacier via L-band airborne SAR tomography," *IEEE Trans. Geosci. Remote Sens.*, vol. 54, no. 12, pp. 7197–7209, Dec. 2016.

[20] A. Linde-Cerezo, M. Rodriguez-Cassola, P. Prats-Iraola, and M. Pinheiro, "Systematic comparison of backgeocoding algorithms for SAR processing and simulation environments," in *Proc. 13th Eur. Conf. Synth. Aperture Radar*, Mar. 2021, pp. 1–4.

[21] A. Benedikter, M. Rodriguez-Cassola, F. Betancourt-Payan, G. Krieger, and A. Moreira, "Autofocus-based estimation of penetration depth and permittivity of ice volumes and snow using single SAR images," *IEEE Trans. Geosci. Remote Sens.*, vol. 60, pp. 1–15, 2022, Art. no. 4303315.

[22] G. Fischer, M. Jäger, K. P. Papathanassiou, and I. Hajnsek, "Modeling the vertical backscattering distribution in the percolation zone of the Greenland Ice sheet with SAR tomography," *IEEE J. Sel. Topics Appl. Earth Observ. Remote Sens.*, vol. 12, no. 11, pp. 4389–4405, Nov. 2019.

[23] G. Fischer, K. P. Papathanassiou, and I. Hajnsek, "Modeling and compensation of the penetration bias in InSAR DEMs of ice sheets at different frequencies," *IEEE J. Sel. Topics Appl. Earth Observ. Remote Sens.*, vol. 13, pp. 2698–2707, 2020.

[24] *Performance Simulator for Bistatic SAR Missions*, ESA, Paris, France, DLR-HR, 4000117230/16/NL/LvH, 2020.

Andreas Benedikter (Member, IEEE) was born in Munich, Germany, in 1994. He received the B.Sc. degree in medical engineering and the M.Sc. degree (Hons.) in electrical engineering and information technology from Friedrich-Alexander University Erlangen–Nürnberg, Erlangen, Germany, in 2017 and 2019, respectively, where he is currently pursuing the Ph.D. degree.

In 2017, he spent one semester at the University of Bristol, Bristol, U.K. Since 2019, he has been a Research Scientist with the Microwaves and Radar Institute, German Aerospace Center (DLR), Weßling, Germany. His research interests include radar signal processing, synthetic aperture radar (SAR) interferometry, radar signal propagation and scattering mechanisms, and the study of future radar concepts, especially in the context of cryospheric applications and planetary exploration missions.

Mr. Benedikter was a recipient of the First Prize of the Student Paper Competition of the IEEE International Geoscience and Remote Sensing Symposium 2023 Conference held in Pasadena, CA, USA.

Marc Rodriguez-Cassola was born in Barcelona, Spain, in 1977. He received the Ingeniero degree in telecommunication engineering from the Universidad Pública de Navarra, Pamplona, Spain, in 2000, the Licenciado (M.Sc.) degree in economics from the Universidad Nacional de Educación a Distancia, Madrid, Spain, in 2012, and the Ph.D. degree in electrical engineering from the Karlsruhe Institute of Technology, Karlsruhe, Germany, in 2012.

From 2000 to 2001, he was a Radar Hardware Engineer with the Study Center of Terrestrial and Planetary Environments (CETP)/French National Centre for Scientific Research (CNRS), Saint-Maur-des-Fossés, France. From 2001 to 2003, he was a Software Engineer with Altran Consulting, Munich, Germany. Since 2003, he has been with the Microwaves and Radar Institute, German Aerospace Center, Weßling, Germany, where he is leading the Synthetic Aperture Radar (SAR) Missions Group. His research interests include radar signal processing, SAR end-to-end simulation, SAR processing and calibration algorithms, crisis theory, and radar mission analysis and applications.

Pau Prats-Iraola (Senior Member, IEEE) was born in Madrid, Spain, in 1977. He received the Ingeniero and Ph.D. degrees in telecommunications engineering from the Universitat Politècnica de Catalunya (UPC), Barcelona, Spain, in 2001 and 2006, respectively.

In 2001, he joined the Institute of Geomatics, Spain, as a Research Assistant. In 2002, he joined the Department of Signal Theory and Communications, UPC, where he worked in the field of airborne repeat-pass interferometry and airborne differential synthetic aperture radar (SAR) interferometry. From December 2002 to August 2006, he was an Assistant Professor with the Department of Telecommunications and Systems Engineering, Universitat Autònoma de Barcelona, Barcelona. In 2006, he joined the Microwaves and Radar Institute, German Aerospace Center (DLR), Weßling, Germany, where he has been the Head of the Multimodal Algorithms Group since 2009. He is the responsible and a main developer of the TanDEM-X Interferometric (TAXI) processor, an end-to-end processing chain for data acquired by the TerraSAR-X and TanDEM-X satellites, which has been used to demonstrate novel SAR acquisition modes and techniques. He is currently involved in the design and implementation of ground processor prototypes and end-to-end simulators of ESA's BIOMASS and ROSE-L missions. His research interests include high-resolution airborne/spaceborne monostatic/bistatic SAR processing, SAR interferometry, advanced interferometric acquisition modes, persistent scatterer interferometry (PSI), SAR tomography, and end-to-end SAR simulation. He has coauthored more than 60 peer-reviewed journal articles in the field.

Gerhard Krieger (Fellow, IEEE) received the Dipl.-Ing. (M.S.) and Dr.-Ing. (Ph.D.) (Hons.) degrees in electrical and communication engineering from the Technical University of Munich, Munich, Germany, in 1992 and 1999, respectively.

From 1992 to 1999, he was with Ludwig Maximilian University, Munich, where he conducted multidisciplinary research on neuronal modeling and nonlinear information processing in biological and technical vision systems. Since 1999, he has been with the Microwaves and Radar Institute, German Aerospace Center (DLR), Weßling, Germany, where he started as a Research Associate developing signal processing algorithms for a novel forward-looking radar system employing digital beamforming on receive. From 2001 to 2007, he led the New Synthetic Aperture Radar (SAR) Missions Group, which pioneered the development of advanced bistatic and multistatic radar systems, such as TanDEM-X, as well as innovative multichannel SAR techniques and algorithms for high-resolution wide-swath SAR imaging. Since 2008, he has been the Head of the Radar Concepts Department, DLR, which currently hosts about 50 scientists focusing on new SAR techniques, missions, and applications. He has been serving as a Mission Engineer for TanDEM-X and he also made major contributions to the development of the Tandem-L mission concept, where he led the Phase-0 and Phase-A studies. Since 2019, he has also been holding a professorship at Friedrich-Alexander-University Erlangen, Germany. He has authored or coauthored more than 100 peer-reviewed journal articles, nine invited book chapters, and about 500 conference papers, and holds more than 20 patents.

Prof. Krieger received several national and international awards, including two best paper awards at the European Conference on SAR, two transactions prize paper awards of the IEEE Geoscience and Remote Sensing Society, and the W.R.G. Baker Prize Paper Award from the IEEE Board of Directors. He has been an Associate Editor of IEEE TRANSACTIONS ON GEOSCIENCE AND REMOTE SENSING since 2012. He served as the Technical Program Chair for the European Conference on SAR and a Guest Editor for IEEE JOURNAL OF SELECTED TOPICS IN APPLIED EARTH OBSERVATIONS AND REMOTE SENSING in 2014.

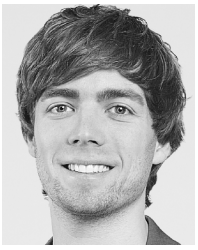

Georg Fischer received the M.Sc. degree in geography from the Ludwig Maximilians University of Munich, Munich, Germany, in 2012, and the Ph.D. degree in environmental engineering from ETH Zurich, Zurich, Switzerland, in 2019.

From 2012 to 2013, he conducted a traineeship at the Mission Science Division, Directorate of Earth Observation Programmes, ESA, Noordwijk, The Netherlands. In 2013, he joined the Polarimetric Synthetic Aperture Radar (SAR) Interferometry Research Group, Radar Concepts Department, Microwaves and Radar Institute, German Aerospace Center (DLR), Weßling, Germany. His research interests include the characterization and modeling of polarimetric, interferometric, and tomographic SAR measurements from snow and ice and the development of methods for the estimation of geophysical properties of glaciers and ice sheets from polarimetric and interferometric SAR data.